

The British University in Egypt

BUE Scholar

Nanotechnology Research Centre

Research Centres

7-22-2022

Flexible humidity sensor based on light-scribed graphene oxide

Mohamed Morsy

mohamed.morsy@bue.edu.eg

Follow this and additional works at: https://buescholar.bue.edu.eg/nanotech_research_centre

Recommended Citation

Morsy, Mohamed, "Flexible humidity sensor based on light-scribed graphene oxide" (2022).

Nanotechnology Research Centre. 29.

https://buescholar.bue.edu.eg/nanotech_research_centre/29

This Article is brought to you for free and open access by the Research Centres at BUE Scholar. It has been accepted for inclusion in Nanotechnology Research Centre by an authorized administrator of BUE Scholar. For more information, please contact bue.scholar@gmail.com.



Flexible humidity sensor based on light-scribed graphene oxide

Emtinan Ouda^{1,*} , Nehad Yousf¹, Mohamed Morsy^{2,3}, and El-Shazly M. Duraia¹

¹ Physics Department, Faculty of Science, Suez Canal University, Ismailia 41522, Egypt

² Housing and Building National Research Center (HBRC), Building Physics Institute (BPI), P.O. Box 1770, 87 El-Tahrir St., Dokki, Cairo, Egypt

³ Nanotechnology Research Centre (NTRC), The British University in Egypt (BUE), Suez Desert Road, El-Sherouk City, Cairo 11837, Egypt

Received: 1 March 2022

Accepted: 29 June 2022

© The Author(s) 2022

ABSTRACT

The light scribe (LS) technique has been applied to reduce graphene oxide (LSGO) over a flexible substrate to be used as a humidity sensor. Graphene oxide (GO) suspension was drop casted over Polyethylene terephthalate (PET) substrate and then reduced inside a conventional light scribe digital video disc (DVD). Interdigitated electrode was precisely fabricated with dimensions of the finger length of 450 μm and width of 20 μm . The prepared material was characterized using X-ray diffraction (XRD), Fourier transform infrared spectroscopy (FTIR), scanning electron microscopy (SEM), and Raman spectroscopy. The results confirm the reduction process of GO using the LS technique. Moreover, the humidity sensing properties of the LSGO was evaluated. Results showed that the present light-scribed humidity sensor has many advantages including rapid response, highly precise due to light scribe technique, and more importantly sensors can be fabricated directly on flexible substrates which are highly favorable for future wearable smart electronics.

1 Introduction

Nowadays, the demand for humidity sensors has rapidly grown day after day for industrial, medical, and home applications [1]. They are used to measure and monitor the amount of water present in the surrounding air. Humidity sensors are available in various types and operate on different principles, such as capacitive [2], resistive [3, 4], semiconductor,

optical [5], and surface acoustic waves. Humidity sensors use different materials, such as metal oxide [6], carbon nanotubes [7], and graphene-based metal oxide [8]. Till now, the commercial market has been dominated by inorganic semiconductor-based sensors due to their reliability and stability. Recently, flexible plastic humidity sensors have great researchers' attention and they appeared as favorable

Address correspondence to E-mail: emtnan_oda@science.suez.edu.eg

candidates for the effective detection and monitoring of various humidity levels [9–12].

The work Mechanism of Reduced graphene oxide humidity sensor is based on its structure where reduced GO has different functional groups on its nanosheets surface. When the water molecule passes through reduced GO nanosheets it will react with the functional groups that exist on its surface. Protons will be generated as a result of this reaction, which leads to reducing the electrical impedance [13]. Since the change in the electrical impedance is significant, reduced graphene oxide can be used to detect the humidity. This mechanism can be explained as the conductivity increases and the relative humidity increases. Proton conduction was proposed a long time ago by Theodor von Grotthuss [14]. Hydrogen ions will diffuse or tunnel into a series of water molecules via hydrogen bonding. The rapid substitution of hydrogen ions takes place between the hydronium cation (H_3O^+) and water molecule [1]. Although the reduced graphene oxide humidity sensors showed promising properties such as the sensitivity and the fast response [15], there are some concerns about the cost and hazards during the reduction preparation process of reduced graphene oxide [16–18].

In 2012, El-Kady [19] and coworkers successfully fabricated an efficient supercapacitor based on reduced graphene oxide using the conventional DVD light scribe drive. The as-fabricated supercapacitor exhibited excellent specific capacitance and high energy density. The authors found that the low-power laser inside the DVD was able to produce exfoliated few-layer graphene nanosheets. Recently, laser-assisted printed sensors attracted tremendous attention due to advantages, such as the low cost of production, easy sample preparation, the ability to process a range of raw materials, and their usability for different functionalities [20, 21].

Acceptable humidity sensors should include some requirements, such as small size, low power, high sensitivity, quick response/recovery time, and operating at lower humidity levels [12]. To achieve these requirements, considerable work has been done. The careful choice of the sensing material is the crucial factor for a good humidity sensor.

The humidity sensing properties of carbon materials at the nanoscale (humic acid) has been studied in our previous report [22]. It has been found that the impedance of humic acid decreases as the relative

humidity increases. The as-fabricated humidity sensor based on humic acid exhibited good sensitivity due to the presence of hydrophilic function groups over the surface of humic acid nanosheets. From this point, the study of LSGO for humidity sensing as another type of carbon nanomaterials was interested to be investigated.

In the present contribution, a cheap and one-step approach has been applied to fabricate a GO nanocomposite over a flexible substrate. The infrared laser inside the commercially known DVD writer was applied to design straight LSGO over a flexible PET substrate. The samples were further characterized by typical characterization techniques such as XRD, FTIR SEM, and Raman to collect information about the morphology and structural characteristics of the synthesized samples. Furthermore, the humidity sensing response of the as-prepared LSGO was tested and evaluated. The humidity was controlled utilizing the saturated salt solutions at room temperature. Based on the acquired results, the fabricated sensor displayed a promising humidity response behavior for both the high humidity range as well as the low humidity range. The current finding is important and opens the gate for future printed detectors over flexible, lightweight, and wearable substrates for the new generation of printed electronics.

2 Experimental work

2.1 Materials

Most chemicals and reagents were obtained from Loba-Chemie PVT-LTD, India. Graphite, sodium nitrate (NaNO_3), hydrogen peroxide (H_2O_2 , 30%), hydrochloric acid (HCl , 35%), sulfuric acid (H_2SO_4 98%), and potassium permanganate (KMnO_4 , 99.3%). The saturated salts are obtained from commercial supplies and used without purification (lithium bromide LiBr , lithium chloride LiCl , potassium carbonate K_2CO_3 , sodium bromide NaBr , sodium chloride NaCl , potassium chloride KCl , and potassium sulfate K_2SO_4).

2.2 Characterization techniques

The structure and crystallinity of the samples were determined using a Philips X-ray diffractometer (Model X-Pert)-utilized monochromatic

($\text{CuK}\alpha = 1.5406 \text{ \AA}$) radiation operated at 40 kV and 25 mA. Changes in surface chemical bonding were characterized using Nicolet 6700 FTIR spectrometer within the range of $400\text{--}4000 \text{ cm}^{-1}$. For more investigation, Raman spectroscopy analysis was studied using a Micro-Raman spectroscopy system (Model Renishaw system 2000) using an Ar+ laser with a power of 100 mW and at the wavelength of 532 nm at room temperature. Surface morphology was investigated using a scanning electron microscope (SEM Model Quantan250 FEG) and optical micrographs were taken with the optical microscope. All measurements were done at room temperature.

2.3 Humidity sensing measurement

The specific response and recovery of the as-obtained LSGO were measured by the LCR bridge at various frequencies varying (50 Hz up to 100 kHz) with different values of relative humidity ranges (7% up to 97%). Maintaining relative humidity levels was accomplished using the saturated solutions method. In this method, the saturated salt solutions were prepared in closed jars [19] to achieve the desired relative humidity (RH) levels in a closed flask using a saturated solution as illustrated in Fig. 1. The saturated salts and the corresponding relative humidity used in this study were LiBr, LiCl, K_2CO_3 , NaBr, NaCl, KCl, and K_2SO_4 to generate 7%, 11%, 23%, 43%, 57%, 75%, and 97% RH, respectively.

2.4 Synthesis of graphene oxide

Graphene oxide nanosheets were synthesized via Hummer's method as reported before [23–25].

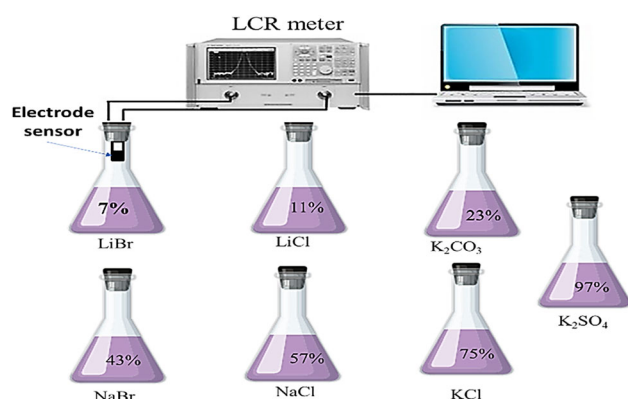


Fig. 1 Illustration of humidity testing measurements using the saturated salt solution method

Briefly, 1.0 g graphite powder was mixed with 0.5 g sodium nitrate (NaNO_3) in 23 ml concentrated sulfuric acid (H_2SO_4). The mixture was vigorously dissolved using a magnetic stirrer in an ice bath to avoid any temperature increment during the reaction. In the next step, 3.0 g of potassium permanganate (KMnO_4) powder was added very slowly under magnetic stirring. After about 2 h the attained mixture was transferred to a warm water bath with an adjustable temperature controller set at 35°C , with continuous stirring for 30 min. Afterward, 92 ml of deionized water (DI) was gradually added, and the solution temperature was kept at 98°C for an additional 30 min. In the final step to terminate the reaction, 140 ml of deionized water was added in addition to 10 ml of hydrogen peroxide.

2.5 Synthesis of light scribe graphene oxide (LSGO)

Graphene oxide 0.5 mg/ml was drop casted over the PET substrate. A distinct pattern region of the graphene oxide film was reduced to form a few layers of graphene using low-energy infrared laser on a commercially available light scribe DVD (HP DVD-R). Laser power was 38 mW with wavelength 780 nm and pixel resolution 600DPI, while the linear velocity was 1.4 m/s. Sure Thing disk labeling software was used to control and design the pattern of LSGO for the humidity sensor. The burning time was about 15 min on average. The best resolution was selected during the burning process. The laser-treated portions changed their color from brownish to dark black color. Finally peeling off patterned PET film from the DVD obtaining several humidity sensors on the PET surface. The fabrication schematic represented in the following figure is also a digital photograph of a flexible laser-scribed micro-device with different bending angles shown in Fig. 2.

3 Results and discussion

Usually, the fabrication process of resistive-type humidity sensors involves several steps including the sensing material preparation and the deposition of electrodes to be able to measure the electrical properties variation as the relative humidity changes [1, 3]. This procedure is not only time consuming but

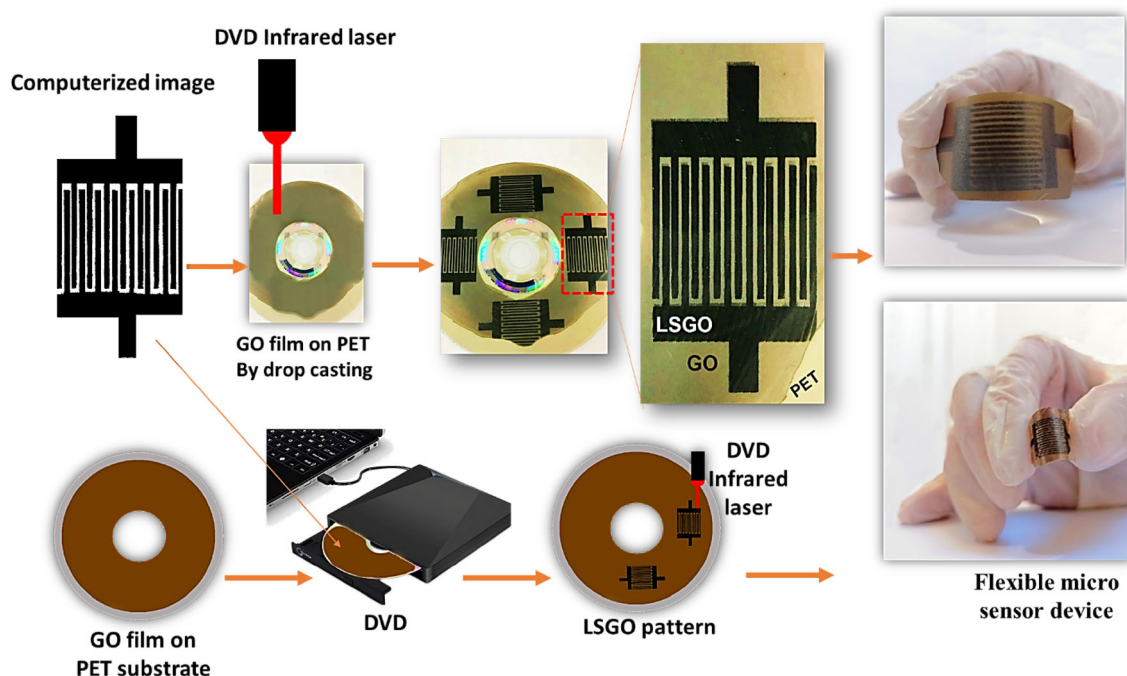


Fig. 2 Schematic diagram showing the fabrication of the humidity sensor based on light scribe graphene oxide (LSGO)

also adds to the cost of the final product. In the present contribution, the light scribe technique was used to prepare a partially reduced graphene oxide layer over PET flexible substrate. The sensor electrode was patterned directly over the graphene oxide layer using infrared laser irradiation. For comparison, two samples have been prepared. The first sample is pure graphene oxide over PET substrate without any laser scribe treatment, while the second one is the GO nanosheets over PET substrate treated by the laser irradiation using the light scribe technique.

3.1 Characterization analysis of GO and LSGO

The prepared samples were characterized by X-ray diffraction to investigate the structural properties (as shown in Fig. 3). For the GO, the XRD pattern shows that an intensive peak has been observed at 2θ equal to 11° related to the (002) plane for graphene oxide. This characteristic peak confirms the oxidation process of graphite. During the oxidation process, function groups intercalated between layers of graphite leading to an increase in the interlayer distance of graphite, so the characteristic peak of graphite at $\sim 26^\circ$ shifted toward 11° and interplanar spacing 0.8 nm which is larger than d spacing of graphite ~ 0.34 nm [24]. The less intensive small peak appeared

at 26.2° is attributed to the unoxidized (not intercalated) graphite (see Fig. 3A).

After applying infrared laser irradiation on GO film, the XRD pattern is significantly changed for LSGO. Where the characteristic peak of GO suffers intensity decreases due to losing some functional groups during the reduction of GO by laser the same results obtained by Huang et al. [26] that change in the (002) peak is shown in Fig. 3B. It is worth mentioning that this explanation will be confirmed through FTIR analysis results of LSGO.

Interplanar spacing was calculated using Bragg's equation: $n\lambda = 2d\sin\theta$ where n is the integer number, d is the distance between the atomic planes, and θ is the diffraction angle ($^\circ$). The crystallite size of materials is calculated using Scherrer's equation [27]:

$$D = \frac{K\lambda}{\beta \cos \theta} \quad (1)$$

where D is the average crystallite size, λ is the x-ray wavelength ($\lambda = 0.154$ nm), and β is the width of the X-ray peak on the 2θ axis, normally measured as the full width at half maximum (FWHM). θ is the Bragg's angle and K is the Scherrer constant ($K = 0.9$). K depends on the crystallite shape and the size distribution, indices of the diffraction line, and the actual definition used for β whether FWHM or integral breadth [28]. Discussion on the accuracy of Eq. (1)

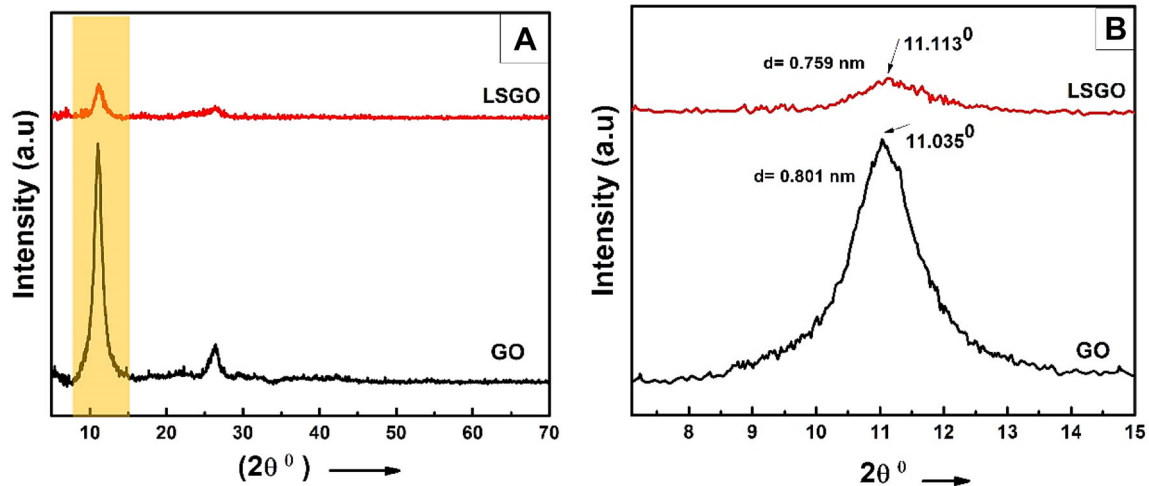


Fig. 3 **A** XRD patterns of pure graphene oxide and light scribe graphene oxide, **B** zoom into the two thetas in the range from 7 to 15 showing the change in the (002) peak

can be found in the literature, for example, in [29]. Moreover, the degree of the crystallinity is determined from the calculated area under the crystalline peaks as follows:

$$X_v(\text{crystallinity}) = \frac{\text{Area}_c}{\text{Area}_c + \text{Area}_n} \quad (2)$$

where Area_c represents the area of crystalline peaks and Area_n represents the area of the non-crystalline peaks. The calculated XRD parameters are shown in (Table 1).

FTIR spectroscopy analysis was done to investigate the structure and functional groups in GO and LSGO (Fig. 4). The FTIR spectrum of GO and LSGO shows a broad peak between 3000 and 3700 cm^{-1} in the high-frequency area corresponding to the stretching and bending vibration of OH groups of adsorbed water molecules. The peaks at 2362 cm^{-1} , 1581 cm^{-1} , and 1039 cm^{-1} were attributed to bending vibrational C–H, the aromatic C=C, and the stretching vibration of C–O, respectively. Therefore, it can be concluded that the samples have strong hydrophilicity. For GO, the characteristic peaks for carboxyl C=O were seen at

1728 cm^{-1} . The oxygen-containing groups in the GO FTIR spectrum reveal that the graphite has been oxidized to form GO. For LSGO the C=O appeared at the same position of GO spectra but showed a much lower intensity (reduced significantly); this change proves that GO reduced to LSGO after the laser reduction of the GO sample. The FTIR results show good agreement with some other reports [30, 31].

The changes in structure from GO to LSGO by laser irradiation are also reflected in the Raman spectroscopy measurements, Fig. 5. Raman spectrum for GO demonstrates a very strong D peak at $\sim 1352 \text{ cm}^{-1}$ with an intensity comparable to that of the G peak at $\sim 1604 \text{ cm}^{-1}$. The Raman spectra of GO indicate D and G peaks. The intense D peak along with a large bandwidth suggests a significant structural disorder in GO [32]. The 2D peak at around 2715 cm^{-1} is attributed to double resonance transitions resulting in the production of two photons with opposite momentum. Unlike the D peak, which is Raman active only in the presence of defects, the 2D peak is active even in the absence of any defects. A defect-activated peak called D + G is also visible at

Table 1 XRD parameters of GO and LSGO samples

Sample	Peak position	FWHM ($^\circ$)	Interlayer distance (d) (nm)	Crystallite size (D) (nm)	Crystallinity (%)
GO	11.035 $^\circ$	1.43386	0.801	4.4	76.5
	26.248	1.40868	3.39106		
LSGO	11.113 $^\circ$	1.39259	0.759	5.8	61.8
	26.063	2.62865	3.41		

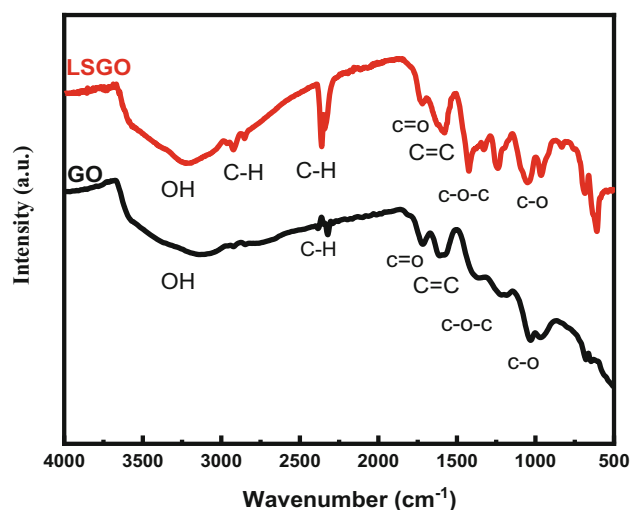


Fig. 4 FTIR spectra of GO and product obtained after light scribe process (LSGO)

around 2935 cm^{-1} . The G peak is due to the bond stretching of all pairs of sp^2 atoms in both the rings and chains. It is the result of in-plane optical vibrations and corresponds to the optical E_{2g} phonons at the Brillouin zone center. The D peak is due to the first-order resonance which represents the breathing mode of aromatic rings arising due to the defects generated in the sample [33]. The D peak intensity is therefore often used as a measure of the degree of disorder.

It should be noted that the wavenumber position of the G and D bands of LSGO is very similar to that observed in the case of the as-prepared GO. During

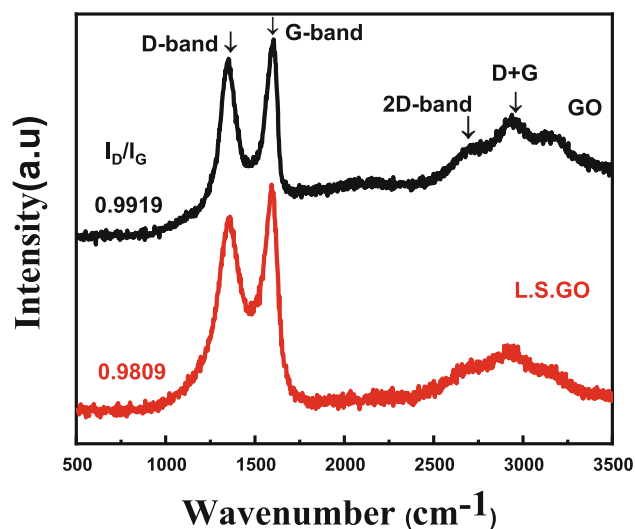


Fig. 5 Raman spectra of GO and LSGO

the reduction process, oxygen and hydroxyl groups would be removed, which is reflected by the change in I_D/I_G ratio [34]. For light-scribed graphene oxide I_D/I_G equals 0.9919; this value is more intense than I_D/I_G of graphene oxide sheet (0.981) due to the formation of a larger sp^2 hybrid region at high temperature. The reason for this is that the removal of oxygen atoms in the reduction process of GO was too intense and it inevitably led to disorder [5, 35]. Using the empirical Tuinstra-Koenig relation [36], the crystallite size (L_a) is also calculated (Table 2).

$$L_a = \frac{2.4 \times 10^{-10} \times \lambda^4}{I_D/I_G} \quad (3)$$

where λ is the wavelength of the excitation laser (in our case $\lambda = 532\text{ nm}$).

SEM images presented in Fig. 6 show the obtained morphology of the LSGO sample. Results indicate the partial exfoliation of layers due to the reduction process, and on the other hand, SEM images in Fig. 7A and B show a thin transparent film of GO nanosheets with relatively large sheet area and characterized by unique wrinkles and folding sheets. Figure 7C illustrates an optical microscope image of LSGO that shows interdigitated finger electrodes. The image includes GO and LSGO. The laser-irradiated area displayed a graphene oxide brownish layer and the color changed to dark black after laser scribed. Judging from the width of the scribed line, the spot size of the laser beam is approximately $20\text{ }\mu\text{m}$. Figure 7E and F shows the finger electrode of LSGO after burning with a light scribe laser more than once. The dark area shows LSGO sheets where the intensity of darkness depends upon the exposure to laser scribe radiation on the DVD many times.

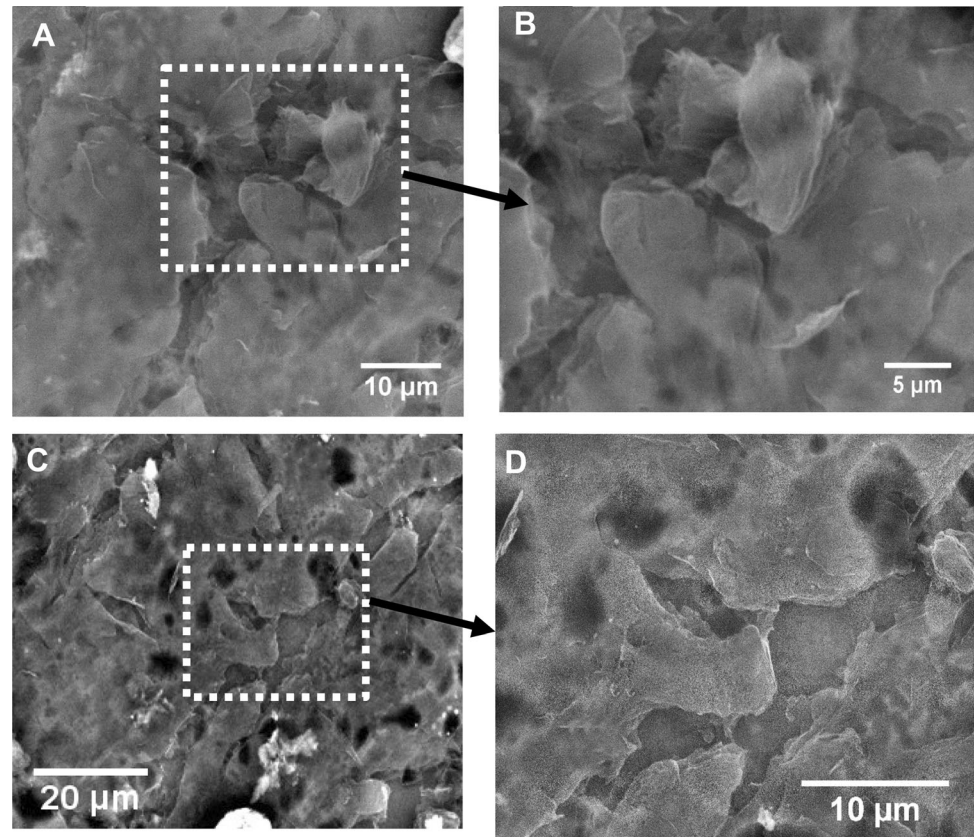
3.2 Humidity sensing performance

The humidity sensing characteristics of the (LSGO) sensor were evaluated in a wide range of relative humidity (7–97%). A saturated salt of LiBr, LiCl, K_2CO_3 , NaBr, NaCl, KCl, and K_2SO_4 was placed for

Table 2 The calculated parameters from Raman spectra

Sample	I_D	I_G	I_D/I_G	L_a (nm)
GO	1580	1348	0.9919	19.06
LSGO	1577	1348	0.9809	18.857

Fig. 6 SEM images of a thick film of LSGO after exposure to the IR laser beam



48 h in some closed flasks to generate 7%, 11%, 23%, 43%, 57%, 75%, and 97% RH, respectively. Before the actual measurements, the fabricated sensor was aged under low and high humidity conditions for 24 h to enhance its stability and increase the signal-to-noise ratio. The sensor was tested by applying 1VAC at different testing frequencies. The impedance variation of the sensor was recorded using a HIOKI-5 LCR meter. The testing frequency is a crucial factor in humidity sensor evaluation, as the sensing characteristics of the humidity sensor rely on the testing frequency. The sensor was tested at a frequency varying from 50 Hz to 100 K Hz at a voltage of 1 V for an additional 24 h. The impedance variation at different testing frequencies is depicted in Fig. 8. As a general trend at all testing frequencies, the impedance decreases as the humidity level increases. The maximum variation in impedance was achieved at 50 Hz. At higher frequency (100 kHz), the impedance variation is insignificant, this is due to the inability of water molecules unable to polarize at higher frequencies [6].

Based on the above results, the sensor was further tested at 50 Hz as the optimum testing frequency.

The normalized sensitivity can be obtained using the following equation:

$$S = \frac{Z_7 - Z_H}{R_H - R_7} \quad (4)$$

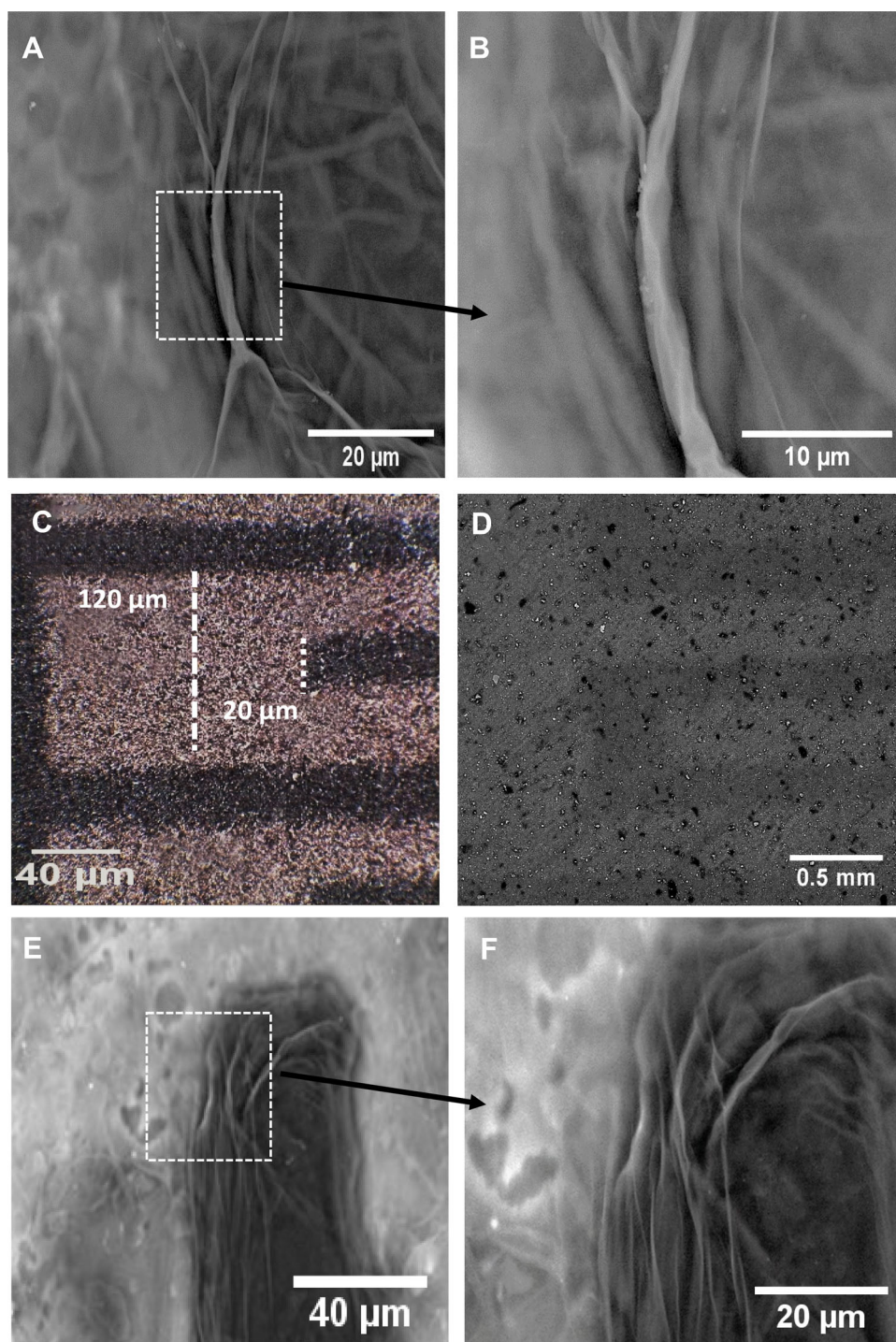
where Z_7 is the impedance value at RH = 7% and Z_H is the impedance value at RH = 97%. The sensitivity has been calculated to be 1.67 MΩ/RH%. The behavior of the tested sensor is described by linear correlation as shown in Fig. 9. The Regression coefficient R^2 is 0.99566, suggesting that the sensor has good linearity.

The difference in the adsorption and desorption process of the humidity sensor is evaluated via hysteresis (H) as expressed in Eq. (5) [37].

$$H = \frac{Z_D - Z_A}{S} \quad (5)$$

where Z_D and Z_A are the impedance values during the desorption and adsorption procedures, respectively. The humidity hysteresis is principally initiated due to the dissimilarity between the adsorption and the desorption of water molecules at the identical RH. The calculations revealed that the sensor has

Fig. 7 Represent **A, B** the GO film before exposure to the laser beam. **C** An optical microscope image of LSGO shows interdigitated fingers electrodes, the dark area corresponds to LSGO, and the light area is GO **D, E, F** for a thin film of LSGO after exposure to the laser beam more than once



maximum hysteresis at 7% RH which reflects the good reversibility of the sensor (Fig. 10).

The humidity sensing mechanism can be reasonably understood using complex impedance spectroscopy (CIS) measurement. The relationship between the real part (Z_{real}) and the imaginary part (Z_{imag}) of impedance in the frequency range from

50 Hz up to 5 MHz at RH% levels of 7%, 75%, and 97% are illustrated in Fig. 11. At low humidity circumstances (7%), the CIS demonstrates a straight line. With an additional increment in the humidity level (43%), the CIS curve has a semicircle. At high humidity levels (84% and 97%), the CIS curve exhibited a line in a semicircle in the low-frequency

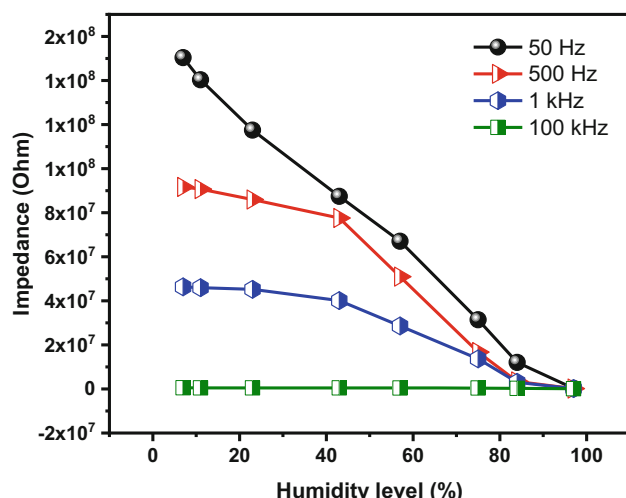


Fig. 8 Impedance versus RH at different testing frequencies

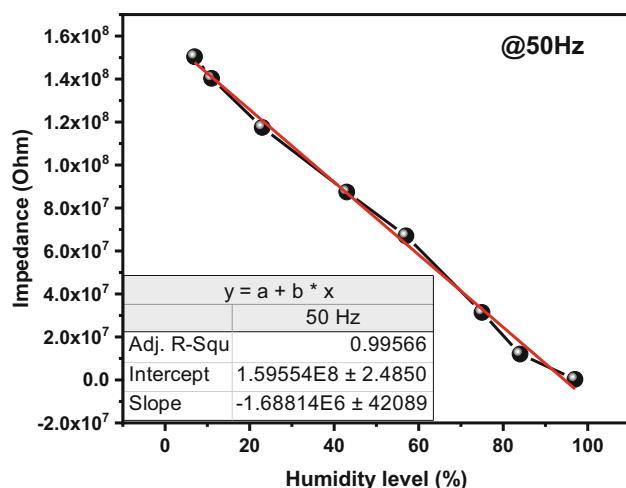


Fig. 9 Impedance versus humidity level at the optimum frequency of 50 Hz. Good linearity was obtained with a fitted line in red color (Color figure online)

region. It was revealed that the shape of the CIS curve specifies the type of conduction. The semicircle is attributed to the inherent impedance of the sensor, while the line at low frequency is owed to the Warburg impedance. The water molecules are physically and chemically adsorbed layer by layer on the surface of the sensing material. At low humidity levels, the water molecules are chemically adsorbed on the surface of the sensor via a double hydrogen bond, which restricts the movement of a water molecule. At this stage, a strong electric field is generated to form hydronium ions (H_3O^+) causing ionization of water molecule (H^+) [38]. With a further increase in humidity level (75%), the ionized H^+ can jump

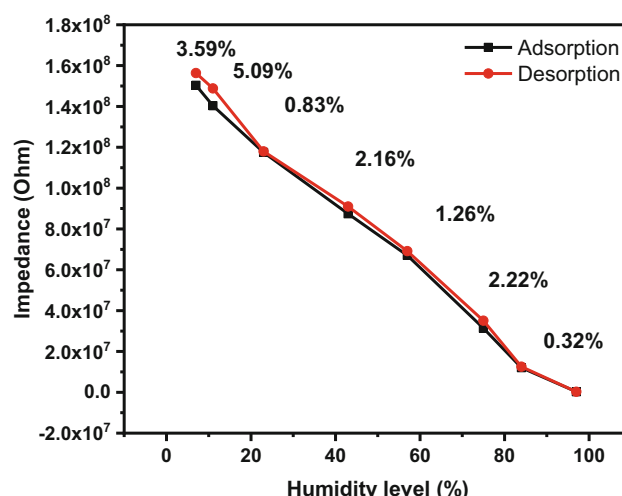


Fig. 10 Impedance versus humidity level in adsorption (black line) and desorption (red line) (Color figure online)

between neighboring water molecules to conduct electricity [8]. This mechanism can be described using the following equation:



With a further increase in humidity level (97%) more water layers are adsorbed and the surface of the sensor tends to be saturated. At this stage, the adsorbed water molecule forms a continuous liquid-like network. The generated H_3O^+ can move freely between adjacent water molecules, leading to a significant decrease in the impedance of the sensor [22, 39–41]. This mechanism is known as the Grotthuss mechanism and can be better described by the following equation:



4 Conclusion

In summary, a flexible humidity sensor based on graphene oxide has been fabricated using a cheap and single-step approach. The low-energy infrared laser used in the commercially known DVD writer was applied to design straight LSGO over a flexible PET substrate. Interdigitated pattern electrodes were precisely drawn by converting graphene oxide into reduced graphene oxide nanosheets. The samples were further characterized by typical characterization

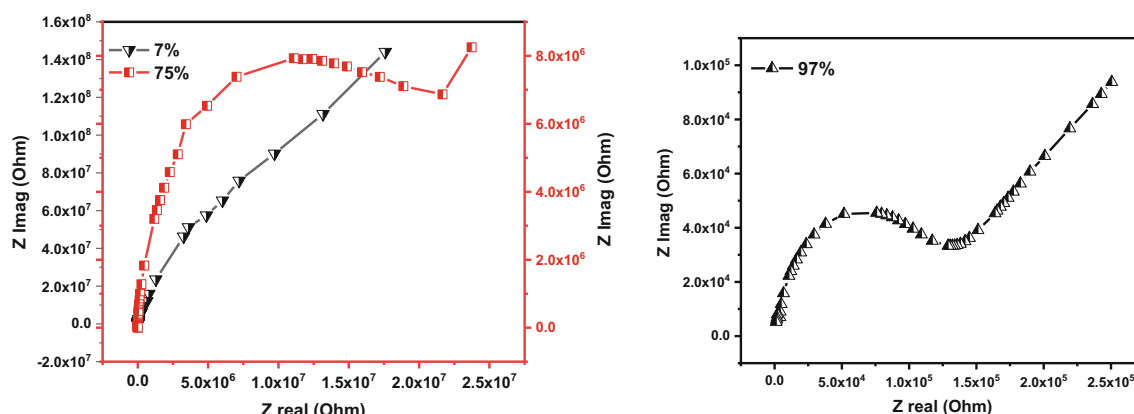


Fig. 11 The relationship between the real part (Z_r) and imaginary part (Z_{im}) of impedance in the frequency range from 50 Hz up to 5 MHz at RH% levels of 7%, 75% (A), and B for 97%

techniques such as XRD, FTIR SEM, and Raman to collect information about the morphology and structural characteristics of the synthesized samples. The humidity sensing behavior of the fabricated sensors was studied in the humidity range from 7% up to 97% RH. Based on the obtained results the humidity sensor exhibited a sensitivity of $1.67 \text{ M}\Omega/\text{RH}\%$. The fabricated sensor demonstrates a low hysteresis of 0.3% at a relative humidity of 84%. The fabricated sensor displayed a promising humidity response behavior for both the high humidity range as well as the low humidity range. The current finding is important and opens the gate for future printed detectors over flexible, lightweight, and wearable substrates for the new generation of printed electronics.

Acknowledgements

The authors would like to thank the academy of scientific research and technology (ASRT), in Egypt for Science Up Grant No. 6583.

Author contributions

All authors contributed to the study conception and design. Material preparation, data collection, and analysis were performed by EO, while NY contributed to the discussion and wrote the study with EO. The humidity measurement and discussion were performed by MM. EMD conceived the original idea and supervised the study. All authors read and approved the final manuscript.

Funding

Open access funding provided by The Science, Technology & Innovation Funding Authority (STDF) in cooperation with The Egyptian Knowledge Bank (EKB). This work was supported by the academy of scientific research and technology (ASRT), Egypt-Science Up Grant No. 6583.

Data availability

The authors confirm that the data supporting the findings of this study are available within the article.

Declarations

Conflict of interest We have no conflict of interest, whatsoever, with anybody.

Open Access This article is licensed under a Creative Commons Attribution 4.0 International License, which permits use, sharing, adaptation, distribution and reproduction in any medium or format, as long as you give appropriate credit to the original author(s) and the source, provide a link to the Creative Commons licence, and indicate if changes were made. The images or other third party material in this article are included in the article's Creative Commons licence, unless indicated otherwise in a credit line to the material. If material is not included in the article's Creative Commons licence and your intended use is not permitted by statutory regulation or exceeds the permitted use, you will need to obtain permission directly from the copyright holder. To view a copy of

this licence, visit <http://creativecommons.org/licenses/by/4.0/>.

References

- H. Farahani, R. Wagiran, M.N. Hamidon, Humidity sensors principle, mechanism, and fabrication technologies: a comprehensive review. *Sensors* (2014). <https://doi.org/10.3390/s140507881>
- S. Ali, M.A. Jameel, A. Gupta, S.J. Langford, M. Shafiei, *Synth. Met.* **275**, 116739 (2021)
- P.G. Su, C.S. Wang, *Sens. Actuators B* **123**, 1071 (2007)
- X. Song, Q. Qi, T. Zhang, C. Wang, *Sens. Actuators B* **138**, 368 (2009)
- W.Y.C. Mahdiar Ghadiy, Mehrdad Gholami, C.K.Lail, Harith Ahmad. *J. Pone* **14**, 1 (2016)
- E.E. Ateia, M.M. Arman, M. Morsy, *Appl. Phys. A Mater. Sci. Process.* **125**, 1 (2019)
- H.W. Chen, R.J. Wu, K.H. Chan, Y.L. Sun, P.G. Su, *Sens. Actuators B* **104**, 80 (2005)
- M. Morsy, M.M. Mokhtar, S.H. Ismail, G.G. Mohamed, M. Ibrahim, *J. Inorg. Organomet. Polym. Mater.* **30**, 4180 (2020)
- S. Li, T. Wan, H. Wei, S. Wang, B. Wang, B. Cheng, *Sens. Actuators B* **362**, 131806 (2022)
- Y. Cheng, H. Wang, L. Li, T. Han, X. Liang, L. Dong, *Sens. Actuators B* **284**, 258 (2019)
- X. Ni, J. Luo, R. Liu, X. Liu, *Sens. Actuators B* **329**, 129149 (2021)
- D. Zhang, M. Wang, W. Zhang, Q. Li, *Sens. Actuators B* (2020). <https://doi.org/10.1016/j.snb.2019.127234>
- E.M. Duraia, G.W. Beal, *Sens. Actuators B* **220**, 22 (2015). <https://doi.org/10.1016/j.snb.2015.05.028>
- R. Pauliukaite, J. Juodkazytė, R. Ramanauskas, *Electrochim. Acta* **236**, 28 (2017)
- Y. Bai, C.Z. Zhang, B. Chen, H. Sun, *Sens. Actuators B* **287**, 258 (2019)
- V. Agarwal, P.B. Zetterlund, *Chem. Eng. J.* **405**, 127018 (2021)
- M. El-Shazly, sibo Duraia, Niu, G.W.Beall, *J. Mater. Sci. Mater. Electron.* **29**, 8456 (2018). <https://doi.org/10.1007/s10854-018-8858-x>
- W. Gary, M. Beall, El-Shazly, QYu. Duraia, Z. d, Liu, *Physica E* **56**, 331 (2014). <https://doi.org/10.1016/j.physe.2013.10.008>
- M.F. El-kady, R.B. Kaner, *Nat. Commun.* **4**, 1475 (2013)
- S.H. Lee, K.Y. Kim, J.R. Yoon, *NPG Asia Mater.* (2020). <https://doi.org/10.1038/s41427-020-0204-0>
- Z. Wan, X. Chen, M. Gu, *Opto-Electron. Adv.* **4**, 1 (2021)
- G.W. Beal, E.M. Duraia, *Sens. Actuators B* **220**, 22 (2015). <https://doi.org/10.1016/j.snb.2015.05.028>
- N. Yousf, E. Ouda, H.S. Magar, R.Y. Hassan, S.A. Mansour, E.S. Duraia, *J. Electrochem. Soc.* **169**, 47518 (2022)
- A.N. Fouda, M.A. Assy, G. El Enany, N. Yousf, Fuller. *Nanot. Carbon Nanostruct.* **23**, 618 (2015)
- E. Ouda, A. Elzwawy, E.S.M. Duraia, *Appl. Phys. A Mater. Sci. Process.* **127**, 676 (2021)
- L. Huang, Y. Liu, L.C. Ji, Y.Q. Xie, T. Wang, W.Z. Shi, *Carbon N. Y.* **49**, 2431 (2011)
- P. Scherrer, *Nachr. Ges. Wiss. Göttingen* **26**, 98 (1918)
- J. I. L. and A.J.C. Wilson, *J. Appl. Cryst.* **11**, 102 (1978)
- V. Uvarov, I. Popov, *Mater. Charact.* **85**, 111 (2013)
- M.L. Yola, N. Atar, Z. Üstündağ, A.O. Solak, *Electroanal. Chem.* **698**, 9 (2013). <https://doi.org/10.1016/j.jelechem.2013.03.016>
- W. Chen, L. Yan, P.R. Bangal, *Carbon N. Y.* **48**, 1146 (2010)
- EshazlyM. Duraia, G.W. Beall, *Superlattices Microstruct.* **98**, 379 (2016). <https://doi.org/10.1016/j.spmi.2016.09.002>
- A.N. Fouda, E.S.M. Duraia, F. El-Tantawy, *Rev. Adv. Mater. Sci.* **45**, 8 (2016). https://ipme.ru/e-journals/RAMS/no_14516/02_14516_fouda.pdf
- S.N. Alam, N. Sharma, L. Kumar, *Graphene* **06**, 1 (2017)
- S. Liu, B. Yu, H. Zhang, T. Fei, T. Zhang, *Sens. Actuators B* **202**, 272 (2014)
- F.Tuinstra and J.L. Koenig, *J. Chem. Phys.* **53**, 1126 (1970)
- W.M. Taha, M. Morsy, N.A. Nada, M. Ibrahim, *Diam. Relat. Mater.* **121**, 108754 (2022)
- M. Pi, D. Wu, J. Wang, K. Chen, J. He, J. Yang, D. Zhang, S. Chen, X. Tang, *Sens. Actuators B* **354**, 131084 (2021)
- S. Kano, N. Jarulertwathana, S. Mohd-noor, J.K. Hyun, R. Asahara, H. Mekaru, *Sensors* **22**, 1 (2022)
- S. Yu, H. Zhang, J. Zhang, *Ceram. Int.* **47**, 30880 (2021)
- M.F. de Aguiar, A.N.R. Leal, C.P. de Melo, K.G.B. Alves, *Talanta* **234**, 122636 (2021)

Publisher's Note Springer Nature remains neutral with regard to jurisdictional claims in published maps and institutional affiliations.